

₁ Preliminary design studies of a drift tube detector for
₂ SHiP experiment

₃ Bereziuk Ivan

₄ September 29, 2015

5 1 Introduction

6 ¹ The completion of the particle content of the Standard Model (SM) with the discovery of the
7 Higgs boson, and advances in cosmology highlight the necessity for a new level of understanding
8 of physics Beyond the Standard Model (BSM). At the same time, neither experiment nor theory
9 provide clear hints of the nature or the scale of this new physics.

10 Over the next decades the Fermi-mass scale, and even beyond, will be comprehensively
11 explored either directly by ATLAS and CMS at the LHC, or indirectly, assuming generic
12 couplings, at experiments like LHCb, Belle2 and NA62 [1]. Hidden particles, which interact very
13 weakly with the SM particles, are predicted in many theoretical models capable of explaining the
14 shortcomings of the SM. A large part of their accessible parameter space remains unexplored.

15 In this situation SHiP is a recently proposed new general purpose fixed target facility at
16 the SPS which is aimed at exploring the domain of hidden particles and make measurements
17 with tau neutrinos. Hidden particles are predicted by a large number of models beyond the
18 Standard Model. The high intensity of the SPS 400 GeV beam allows probing a wide variety
19 of models containing light long-lived exotic particles with masses below $10 \text{ GeV}/c^2$, including
20 very weakly interacting low-energy SUSY states.

21 1.1 Overview of the Experiment

22 At the energy accessible at the SPS, the hidden particles are predominantly produced in decays
23 of hadrons, in particular in decays of charmed and beauty hadrons above the kaon mass, and
24 in proton bremsstrahlung.

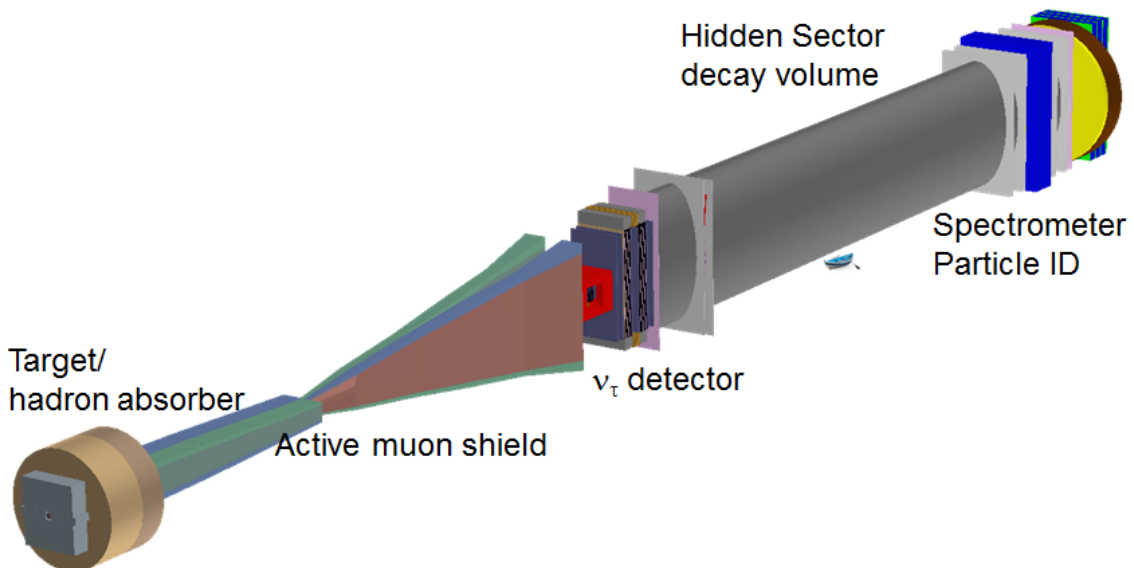


Figure 1: Overview of the SHiP facility [2]

¹This section mostly(The information of for this section was) taken from SHiP Technical Proposal (TP) document [2] just to overview the experiment and prepare reader for subsequent work under separate part of detector.

25 The detector for the direct detection of the hidden particles is designed to fully reconstruct
 26 their exclusive decays. Table 1 summarizes the main decay modes of the hidden particles in
 27 the various models considered.

Table 1: Summary of the main decay modes of hidden particles in various models ($\ell = e, \mu$).

Models	Final states
Neutrino portal, SUSY neutralino	$\ell^\pm\pi^\mp, \ell^\pm K^\mp, \ell^\pm\rho^\mp, \rho^\pm \rightarrow \pi^\pm\pi^0$
Vector, scalar, axion portals, SUSY sgoldstino	$\ell^+\ell^-$
Vector, scalar, axion portals, SUSY sgoldstino	$\pi^+\pi^-, K^+K^-$
Neutrino portal ,SUSY neutralino, axino	$\ell^+\ell^-\nu$
Axion portal, SUSY sgoldstino	$\gamma\gamma$
SUSY sgoldstino	$\pi^0\pi^0$

28 The principal background to the hidden particle decay signal originates from the inelastic
 29 scattering of neutrinos and muons in the vicinity of the detector producing long-lived particles.

30 The beam line is designed to minimize the background sources. The proton interaction in
 31 the target gives rise to a copious direct production of short-lived resonances, pions and kaons.
 32 While a hadron stopper of a few metres of iron is sufficient to absorb the hadrons and the
 33 electromagnetic radiation emerging from the target, the decays of pions, kaons and short-lived
 34 resonances result in a large flux of muons and neutrinos. In order to reduce the flux of neutrinos,
 35 in particular the flux of muon neutrinos and the associated muons, the pions and kaons should
 36 be stopped as efficiently as possible before they decay. The target must therefore be made of
 37 a material with the shortest possible interaction length and be sufficiently long to contain the
 38 hadronic showers with minimum leakage. Since the production angle of the hidden particles is
 39 relatively large, there is no requirement to minimize the beam spot.

40 The short-lived resonances and the residual flux of decaying pions and kaons still give rise to
 41 a large flux of muons. This flux must be efficiently cleared from the detector fiducial volume by
 42 either a passive shield or through an active shield based on magnetic deflection. The residual
 43 flux should also be low enough so not to compromise the occupancy limit in the tau neutrino
 44 detector. As illustrated in Figure 1, in the baseline design a 5 m horizontally wide region
 45 respecting these requirements has been achieved with a 48 m long active muon shield based on
 46 magnetic deflection of the muons in the horizontal plane.

47 The muon shield is followed by the 10 m long tau neutrino detector, which puts the start of
 48 the HS decay volume at about 64 m [2]. The main purpose of the tau neutrino detector is to
 49 perform the first direct observation of the $\bar{\nu}_\tau$, and to study the properties and the cross section
 50 of ν^τ and $\bar{\nu}_\tau$. The current optimization of muon shield and cost, results in a decay volume with
 51 an elliptical shape of 5 m width and 10 m height. The length of the decay volume is obtained
 52 by maximizing the acceptance to the hidden particle decay products given the transversal size.

53 The full reconstruction of the hidden particle decays requires a magnetic spectrometer and
 54 a system for particle identification at the end of the decay volume.

55 The particle identification system requires an electromagnetic calorimeter for e/γ identifica-
 56 tion with sufficient granularity and energy resolution in order to reconstruct π^0 's, and a hadron
 57 calorimeter in combination with a muon detector for π/μ separation.

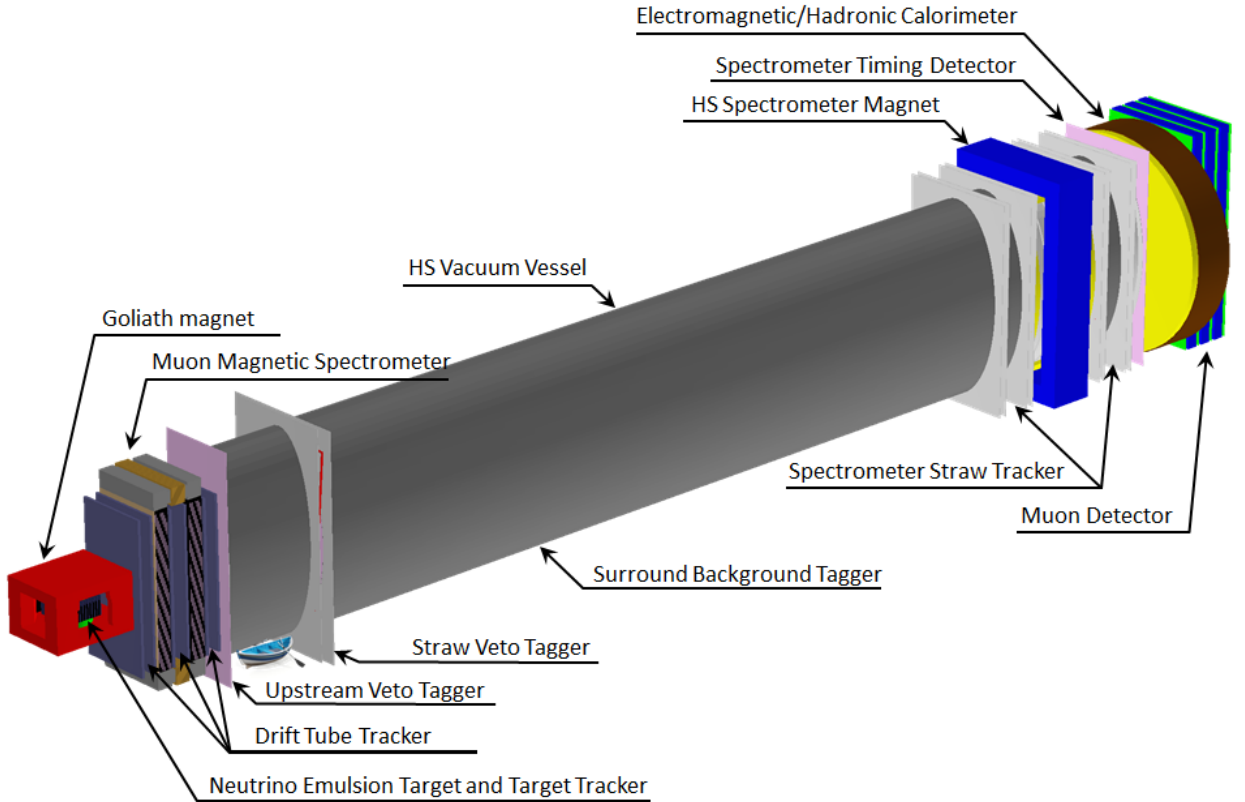


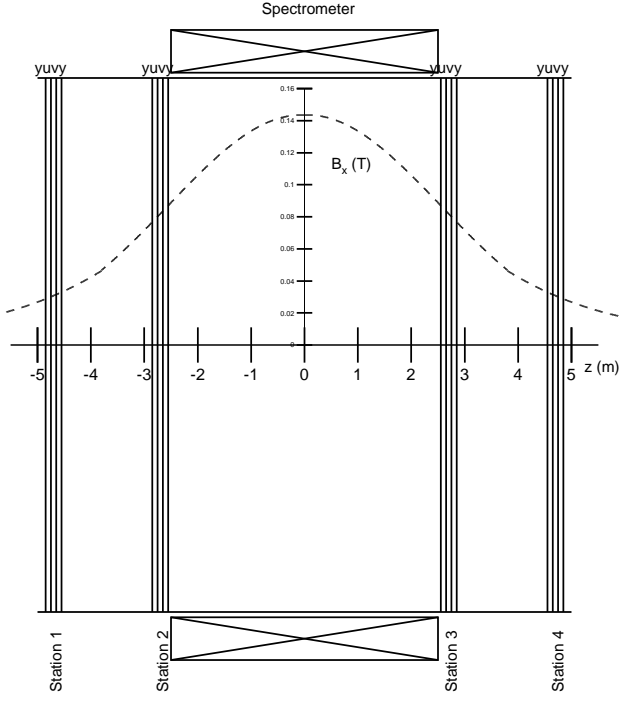
Figure 2: SHiP detector layout

58 1.2 Spectrometer tracker

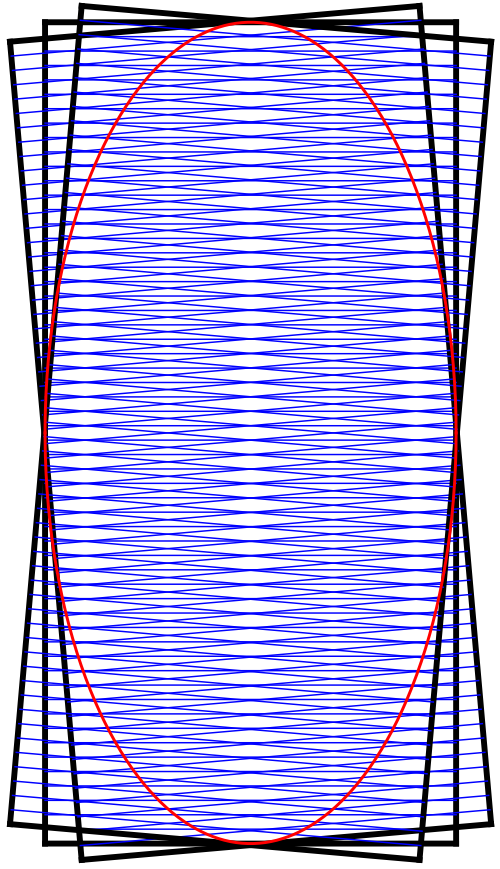
59 Spectrometer tracker is a part of particle identification system. The purpose of the HS spec-
 60 trometer is to reconstruct with high efficiency the tracks of charged particles from the decay
 61 of hidden particles. The spectrometer must provide an accurate determination of the track
 62 momentum and of the flight direction within the fiducial decay volume.

63 The spectrometer consists of a large aperture dipole magnet and two tracking telescopes on
 64 each side of the magnet. A layout with four tracking stations symmetrically arranged around
 65 the dipole magnet, as depicted in Figure 3a, is taken as a baseline. The size and layout of the
 66 tracker stations is connected to the size of the magnet. A dipole spectrometer magnet with a
 67 horizontal gap of 5 m, a height of 10 m and a length of 5 m provides good acceptance coverage
 68 and is considered feasible at a reasonable cost.

69 Following the direction of the magnetic field, the measuring elements are oriented horizon-
 70 tally to measure precisely the vertical (Y) coordinate. Two stereo views (U and V) are rotated
 71 by an angle $\pm\theta_{stereo}$ for measuring the transverse coordinate X with an accuracy degraded by
 72 $\sim 1/\sin\theta_{stereo}$. The precision in X (i.e. the value of the stereo angle) is driven by the need
 73 of a good enough measurement of the decay vertex, opening angle of the daughter particles
 74 (which enters the invariant mass) and impact parameter at the production target. Each station
 75 contains 4 views (Y-U-V-Y). The two stations on the same side of the magnet are separated by
 76 $\Delta = 2m$ and a gap of 5m is left between the second and third stations (i.e. each is 2.5m away
 77 from the centre of the magnet).



(a) Position of the tracking stations and dipole magnet, overlaid with magnetic field component B_x as a function of z .



(b) Four views in one station (not all straws shown, for the sake of clarity). The nominal acceptance, defined by the vacuum vessel, is shown as a red ellipse.

Figure 3: Spectrometer layout

The tracking stations of the magnetic spectrometer must provide good spatial resolution and minimise the contribution from multiple scattering. In addition, the tracker must operate in vacuum. A straw tracker made of thin polyethylene terephthalate (PET) tubes is ideal to meet these goals. Gas tightness of these tubes has been demonstrated in long term tests and the mass production procedure is also well established (see NA62 experiment [1]). The main differences between the SHiP tracker and the NA62 tracker are the need for 5 m long straws (vs 2.1 m in NA62). The main changes with respect to the Expression of Interest [6] follow from the changes applied to the spectrometer magnet. The straw orientation has been turned from vertical to horizontal and one transverse dimension has been increased from 5 to 10 m.

2 Subject of study

With new requirements for new straw tracker we have important challenge for long straws. It is related with the fact that straw and wire will be subjected to gravitational and electrical

90 forces and it causes the sagging. Because the straws are oriented horizontally (or almost, in
91 case of stereo views), sagging is expected to cause in most drift tubes a downward deflection,
92 which might be exploited when applying a correction.

93 Undoubtedly the presence of sagging can complicate the data processing stage and somewhat
94 worse accuracy of track reconstruction. Primary question we have to investigate "is acceptable
95 sag-admitting design?" and "What a downgrade of precision for sag-admitting design?".

96 Results of measurements on prototypes are discussed in Section 8.

97 3 Signal

98 Computer program Garfield [3] is designed for detailed simulation of two- and three-dimensional
99 gas detectors. So we will perform STRAW tube studies using this program.

100 Charged particle create electron-ion pairs while traverse the drift tube. Electrons under
101 affecting the electric field drift to the wire anode (see Fig.4). During the travel they increase
102 their energy and invoke an avalanche. Therefore they produce a measurable signal.

103 Initial electrons drift to the wire due to the electrical field between the wire and the tube
104 wall. Electrons ionize gas molecules due to the high electric field around the wire, especially
105 near the wire when the strength of the electric field becomes very large. Subsequently readout
106 electronics process the signal induced on the wire.

107 The event is registered if signal reach some a threshold voltage (Fig. 5). So the value of
108 threshold is a key factor on the way of searching optimal setting for signal processing procedure.

Table 2: STRAW tube parameters

parameter name	value
wire	$30 \mu m$ gold-plated Tungsten
straw length	5 m
voltage	1750 V
inner tube radius	9.8 mm
wire medium density	$19.3 g/cm^3$
wire tension	$\sim 90 g$
working tube gas mixture	Ar 70% CO_2 30%

109 We have to set threshold as low as possible but enough above from noise level to achieve
110 best rate of true/false detected tracks and highest track registration precision and efficiency.

111 A variation of the signal height introduces a variation in the time when the signal passes
112 the threshold and is considered to be the main contribution to the STRAW tracker resolution.

113 In the track reconstruction software(GARFIELD [3]) an effective TR-relation is used. It only
114 describes the relation between the drift time and the distance from the track to the wire, which
115 differs from the distance to the ionization cluster. The shape of the TR-relation is defined by
116 the drift velocity of the ionization cluster inside the straw. The electric field increases towards
117 the wire, leading to a non linear TR-relation.

118 The drift time versus the unbiased distance distribution and the result of the fit are shown
119 in Fig. 17a. Noise hits under the main distribution, i.e. at earlier times, are due to primary
120 or secondary particles (δ -rays) passing the straw at a closer distance to the wire, consequently

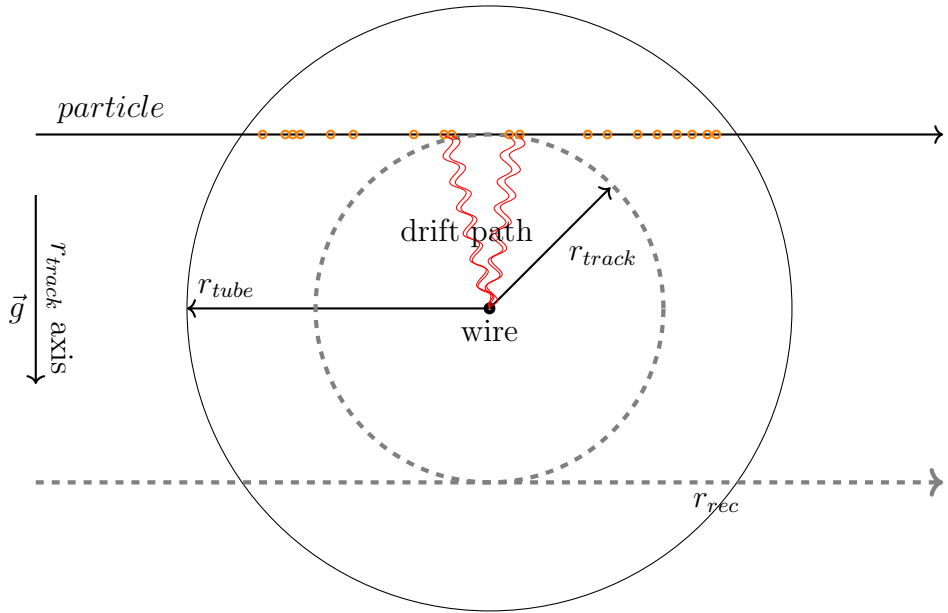


Figure 4: Schematic view of a particle passing the straw and producing ionization clusters (orange points). Electrons of ionization cluster drift to the wire and induce the signal. The closest distance from the track to the wire, r_{track} , and radius of the straw, $r_{tube} = 2.45\text{mm}$, are also indicated.

¹²¹ producing an earlier signal. Initial clusters along the track are marked by orange points in the
¹²² figure.

¹²³ Muon μ was chosen as test particle for simulation with energy 1GeV . You can see some of
¹²⁴ typical tracks from the μ through the tube Fig.10a,10b.

¹²⁵ 3.1 Leakage noise

¹²⁶ Every time we deal with different kind of noise. Basically it is noise from leakage current
¹²⁷ through readout electronics.

¹²⁸ As will be discussed further we analyse not the current invoked by particle but the output
¹²⁹ voltage from amplifier. In GARFIELD we able convolute input current $I(t)$ with electronic
¹³⁰ response function (1)²

$$f_{resp} = A \cdot (e^{-t/0.005} - e^{-t/0.030}) \quad (1)$$

¹³¹ Noise is very important for every calculations and it makes bit impact on straw precision
¹³² and straw efficiency. So we can't rely on results until we receive signal and noise from real
¹³³ STRAW tube prototypes.

¹³⁴ Convolution of input current makes it smooth. Usually in typical conditions³ noise have
¹³⁵ gauss distribution with RMS equal to a amplitude of signal from 2000 electron in the tube -

²in this equation t in nanoseconds

³as in table 2

¹³⁶ electric noise charge (ENC)⁴ On Fig.5 you can see deposition from noise marked by blue line.
¹³⁷ On the Fig.5 the timestamp *Time* = 0 corresponds to the time when muon hits a tube.
¹³⁸ The convolution function smooths and spreads input current. It mean that the output voltage
¹³⁹ in GARFIELD does not contain part of signal before hit event timestamp.

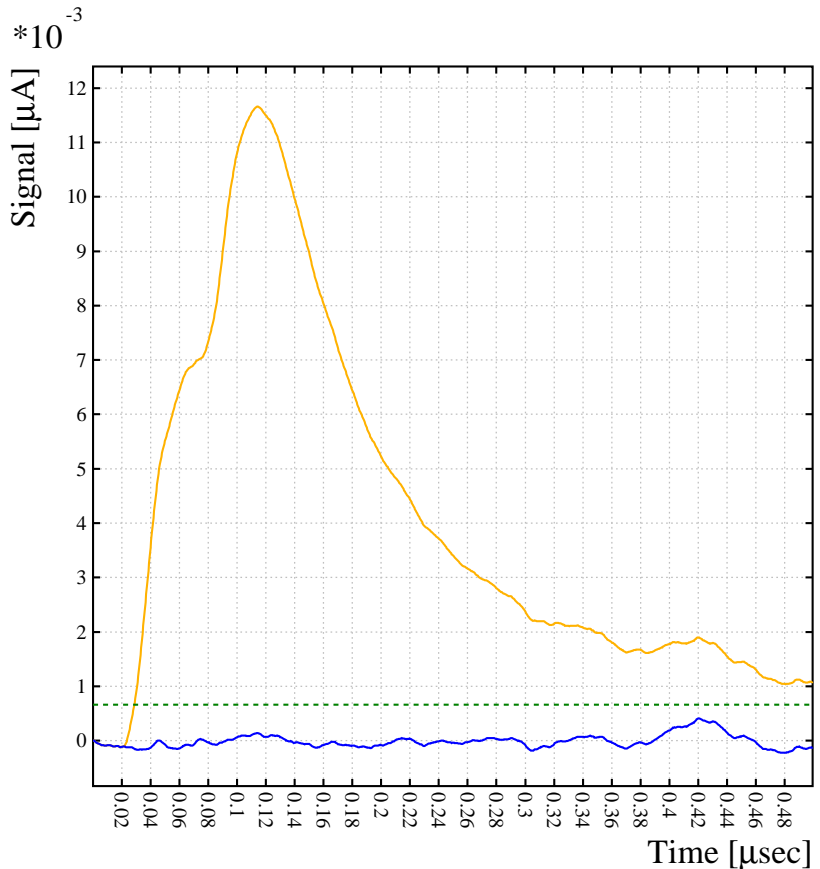


Figure 5: Example of output signal $V(t)$ after convolution (front-end electronics) from central track (yellow line). The noise component of the same signal depicted by separate blue line. Grin dashed line is a threshold for triggering drift time and equals to 5σ of noise distribution.

¹⁴⁰ 3.2 STRAW efficiency

¹⁴¹ The interaction of charge particle with gas molecules has probabilistic nature. For short dis-
¹⁴² tance tracks (somewhere near the tube wall) the probability of tracks that generation of zero
¹⁴³ electron/ion pairs becomes significantly high.

¹⁴⁴ The number of produced ionization clusters directly affects the hit efficiency profile. Smaller
¹⁴⁵ ionization length increases the hitting efficiency because of production more ionization clusters
¹⁴⁶ per length unit [4]. In GARFIELD we can easily calculate amount of clusters per track. In

⁴With testing of real 5 m long straws and ultimate examples of electronics we will measure real noise. But for now it is only close to reality suggestion concerning to this issue.

¹⁴⁷ Fig.7b you can see a distribution of number of clusters per central track for our STRAW tube.
¹⁴⁸ It means that straw efficiency will be lower near the tube wall (see Fig.6).

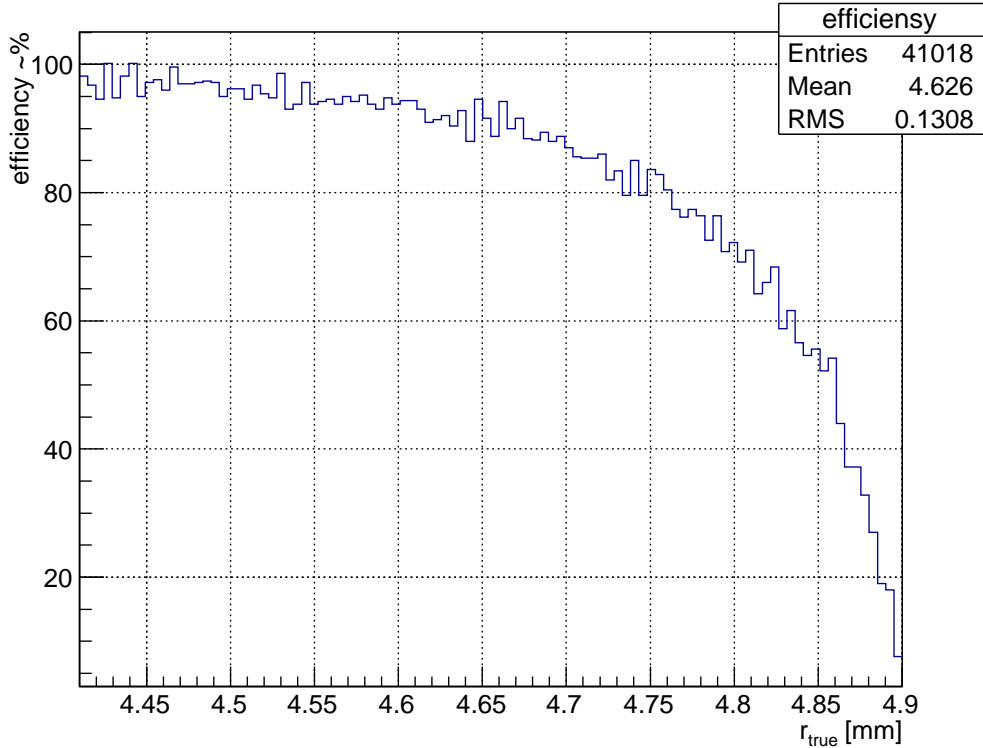


Figure 6: Straw tube efficiency. Result of homogeneous penetrating periphery of tube by 50k events (scaled down by factor of 5. $\frac{50k \text{ events}}{100\text{bin}} = 500 \frac{\text{events}}{\text{bin}}$).

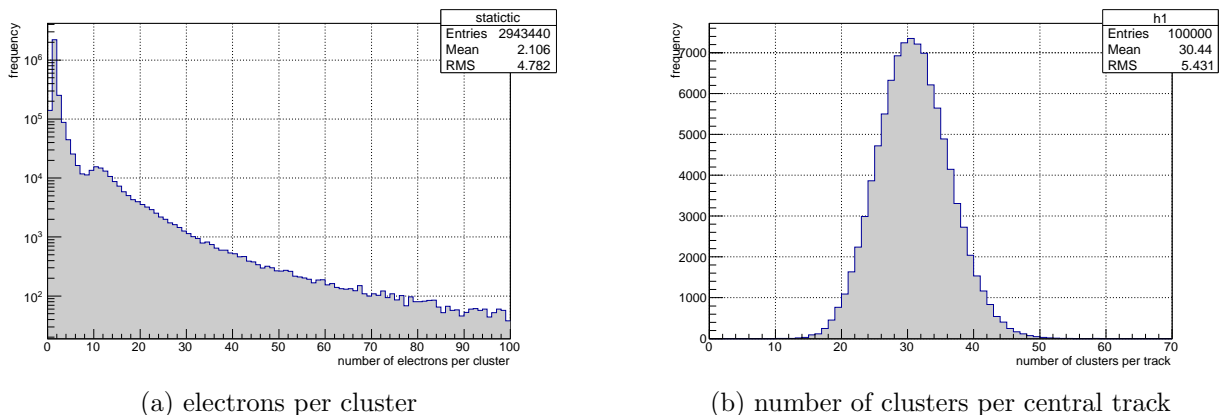


Figure 7: Statistics info from GARFIELD about track from $1GeV \mu$. Tube described in table 2

¹⁴⁹ From the Fig.6 we can conclude that the efficiency of tube is 100% almost in whole region

150 covered by tube except pre wall region which is quite small. Increasing the gas mixture density
151 or increasing the tube radius for the same gas density can increase tube efficiency.

152 4 Gain

153 Lets look on avalanche process in the tube. If multiplication occurs, the increasing of the
154 number of electrons per path ds is given by

$$dN = N\alpha ds \quad (2)$$

155 The coefficient α is determined by the excitation and ionization cross sections of the elec-
156 trons that have acquired sufficient energy in the field. It also depends on the various transfer
157 mechanisms and electric field E and increases with the field because the ionization cross-section
158 goes up from threshold as the collision energy ε increases. As we can suppose the coefficient α
159 is of big amount of parameters.

160 The amplification factor G on a wire(that is more interesting for us) is given by integrating
161 (2) between the point s_{min} where the field is just sufficient to start the avalanche and the wire
162 radius a :

$$G = N/N_0 = \exp \int_{s_{min}}^a \alpha(s) ds \quad (3)$$

163 GARFIELD can provide us by amplification factor G for any point of the tube(because G
164 is coordinate dependent magnitude). The amplification factor is equal almost in whole tube
165 space except neighbourhood near the wire because electric field becomes significantly high only
166 near the wire (see figs 8a, 8b). When the wire is shifted from the center of the tube the electric
167 field in area close to the wire is the same as in centered state. So the amplification factor G is
168 quite similar in both cases.

169 Implementation of gain value calculation is not so reliable in GARFIELD(especially for-
170 tran version). Gain should be recalculated using Garfield++ (which is newer and takes into
171 consideration more effects).

172 On the Fig.9 you can see that the gain $G(V)$ have precisely exponential dependence. This
173 is frankly does not inspire confidence. The difference can be up to 100% (as Rob Veenhof -
174 creator of GARFIELD [3] said).

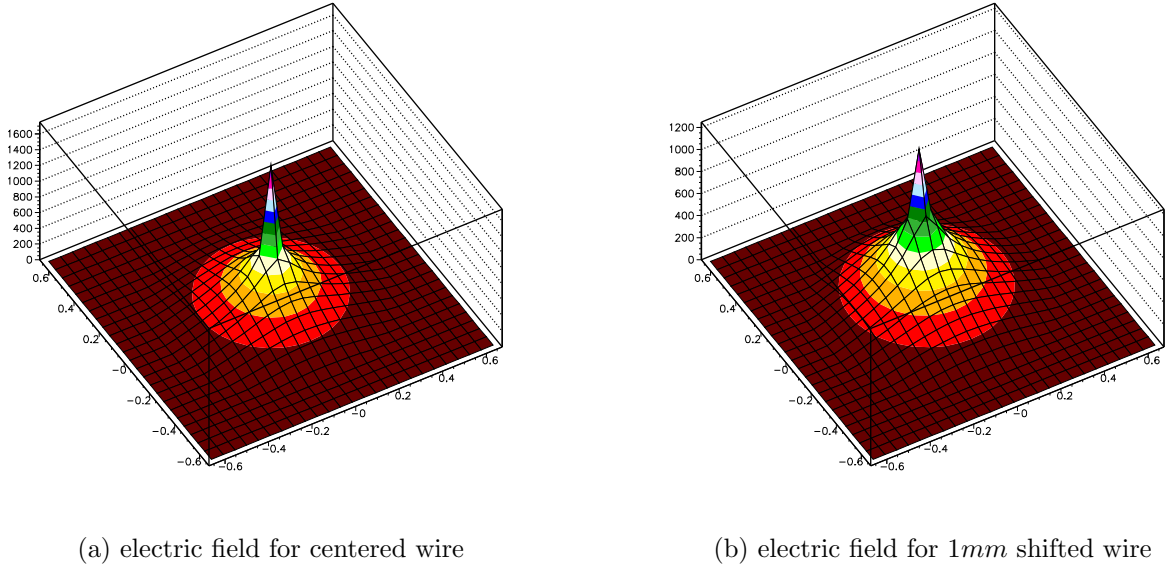


Figure 8: Electric field intensity map for different wire position in the cube calculated in GARFIELD software. Conditions for those plots are described in table 2

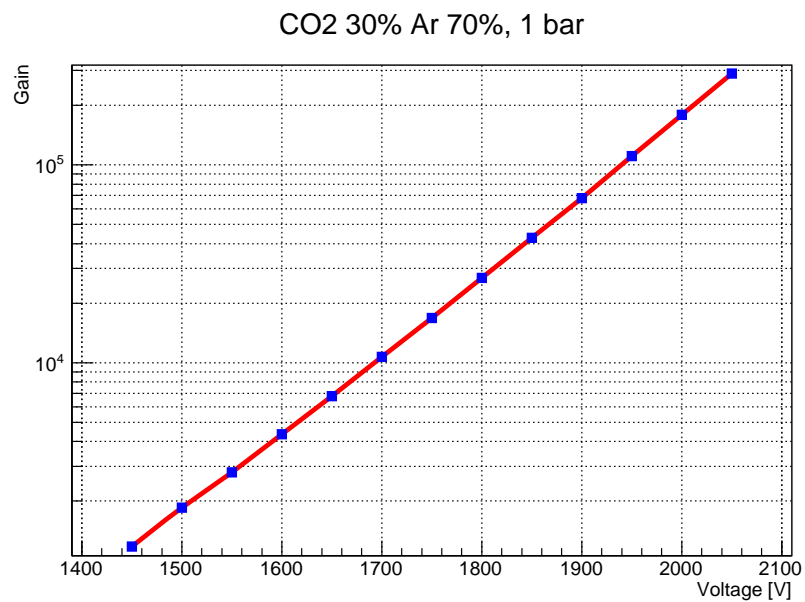


Figure 9: Dependence of the gain of the voltage applied to the wire. The rest of STRAW tube settings corresponds to table 2.

175 5 Wire sagging

176 Easy to predict that the displacement of the wire invokes distortion an electric field (see
 177 figs 8a,8b) and drift path for electrons/ions inside the tube (see fig.10a and Fig.10b). The
 178 RT-relation for track reconstruction directly depends on the wire position in the tube. So
 179 RT-relation loses it's previous symmetry (see next sections).

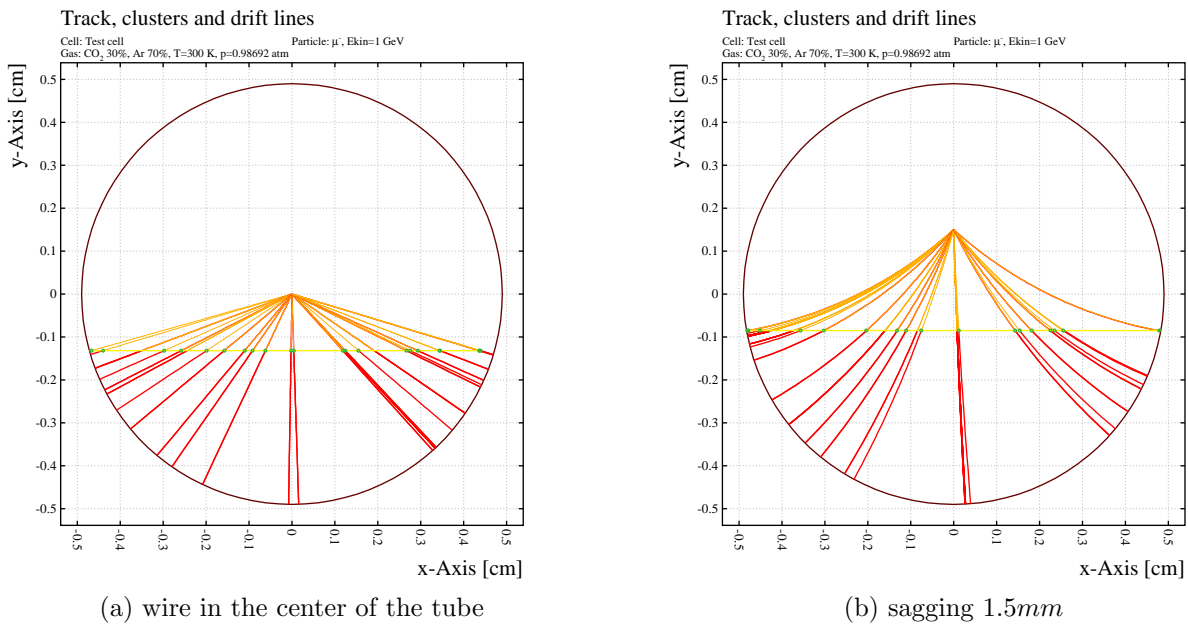


Figure 10: An example of tracks from the on the tube for different position of the wire from GARFIELD simulations. Initial clusters marker by green. Drift lines for electrons marked by yellow, ions – red lines.

180 The direction of sagging is unpredictable when the wire is centered and the straw has vertical
 181 orientation. Impact of gravitation field into the wire does not make any effect in this state.
 182 But we can avoid this ambiguity by setting straws horizontally. This condition is necessary
 183 to make track reconstruction possible. Even when strung with a pulling force T close to the
 184 breaking limit, wires in several metre long tubes will experience a gravitational sag that is large
 185 in comparison with the achievable accuracy of drift tubes.

186 We estimate significant wire sagging(by comparison to the tube radius) because of wire
 187 attraction to the tube under affecting of gravitation and electric field force.

188 You can see a profile of wire sagging of 5m length wire in 1cm diameter straw tube and
 189 1750V voltage on the Fig.11 calculated in GARFIELD software [3].

190 The calibration of STRAW tube with sagged wire is more difficult by comparison to the
 191 mode without sagging.

192 Variation of wire tension, wire radius should be taken into account as high affect factor for
 193 sag value.

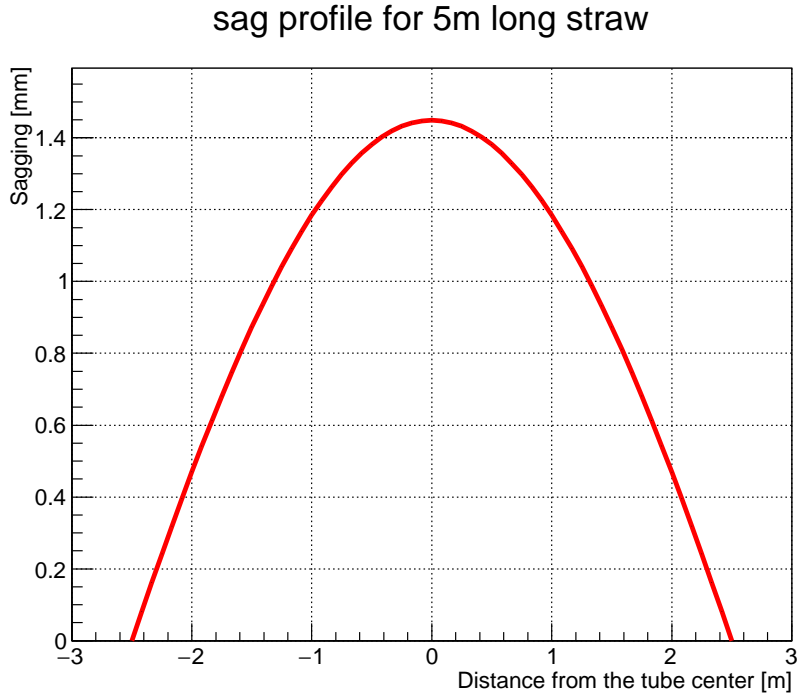


Figure 11: Wire sag profile under electric and gravitation field calculated in GARFIELD. All options for this straw system are described in table 2.

194 6 Sag estimation

195 In this section we have to find out method for assessing sagging. This is key step that makes
 196 track reconstruction procedure possible.

197 At first we have to think on data we can use for such kind of calculations. We can extract
 198 much useful information from drift time distribution.

199 The wire sags under electric and gravitation force. Therefore the sag value differs along
 200 the tube (Fig.11). But we can separate collected data for different position along the tube.
 201 STRAW tube detector consists of several parallel layers of tubes at some angle to each other.
 202 So we can easily fix longitudinal position (along the tube) for tracks that cross several crossed
 203 tubes (at least two). Collimation is also possible via scintillator triggering before and after
 204 STRAW tube.

205 Lets say we can install our STRAW tube into homogeneous particle flow and save drift time
 206 distribution for some narrow section of the tube. These distributions are different from each
 207 other(see example on Fig.12). The difference between diagrams increasing with sag difference.
 208 So it is good tools for sag calibration.

209 Then we have to bind each drift time distribution with appropriate sag value. This is part
 210 of laboratory work when sag profile measurements can be performed via optical method prior
 211 to the exposition.

212 GARFIELD can handle only two-dimensional tasks. So every simulation in this article is
 213 plane - as shown in Fig.10a. Distributions on Fig.12 contains GARFIELD simulations for tube
 214 with wire located at certain position (in terms of displacement from tube center).

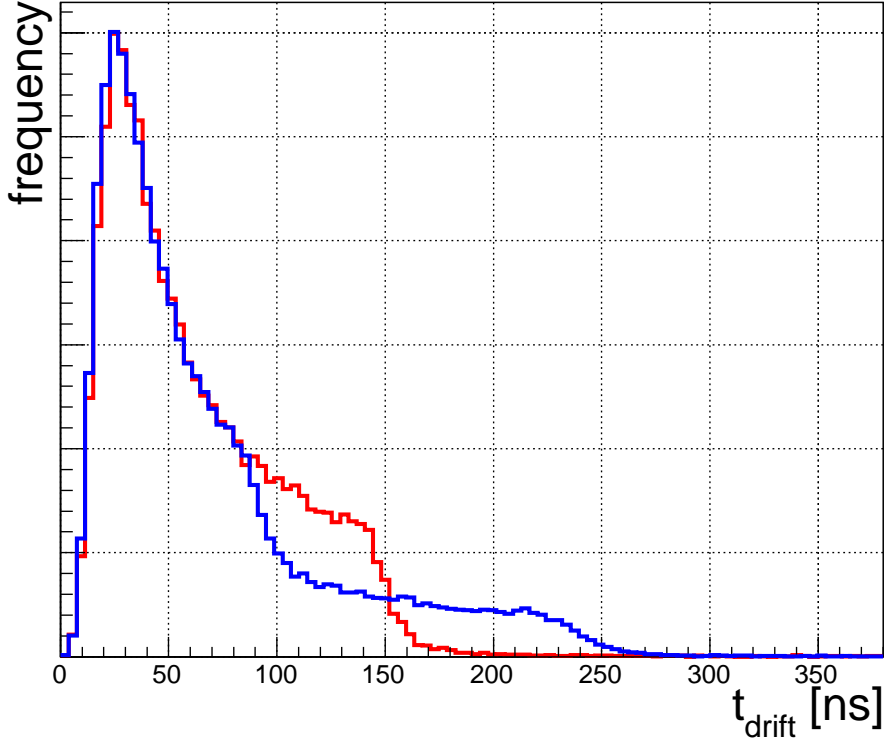


Figure 12: Drift time distribution for a homogeneous irradiation with a centered wire (red) and for a wire offset of 0.9 mm (blue).

Lets say we have an equipment for scanning the tube to measure wire sagging profile. After profile measurements we divide our tube into sections. Wire position within separate section should be defined within desired precision

So we need divide our tube on 57 sections (see Fig.13) if maximum of wire offset (at the center of the tube) is equal to 1.45mm and desired precision is 50 μ m.

$$N_{halftube} = \frac{1.45\text{mm}}{50\mu\text{m}} = 29; \quad (4)$$

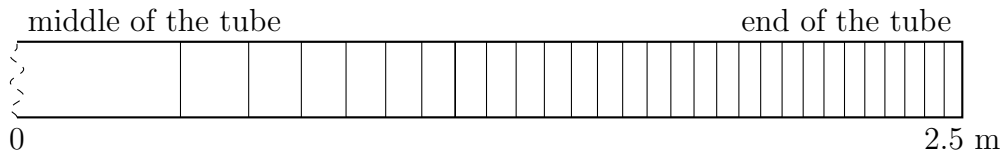


Figure 13: Tube sectioning. Sag value at the tube center is 1.45mm. Difference of wire sag value from section to section is 50 μ m

Then we need to make an exposition with sufficient number of events for every of sections (at least 50k events per section). Time of exposition can reach very high values for close to the tube end sections because of small area of exposition.

223 The next step is to find dependence of DT-distribution shape with wire offset. The point
224 that we can evaluate matching between histograms via χ^2 criteria. As we can see in the Fig. 14a
225 the comparison of χ^2 has smooth dependence across increasing of wire offset for high statistic
226 histograms.

227 First steps for sag estimation are:

- 228 1. measure wire sag profile via optical method;
- 229 2. make a sectioning of tube due to wire sag profile;
- 230 3. collect enough amount of events for every of dt-distribution and save this *core* distribution
231 for further comparisons.
- 232 4. measure DT-distribution of tube section that is subject of study and adjacent area.
- 233 5. calculate χ^2 criteria for this current dt-distribution with each of core distribution.
- 234 6. correlate found values of wire displacement relatively to the adjacent sections or by fitting
235 of whole wire profile points.

236 **6.1 Finding most probable value of wire displacement for certain 237 point of the tube**

238 **6.2 Raw method**

239 The simplest method to find S is to equate it to the corresponding value of best matched core
240 DT-histogram.

241 On the figure 14b you can see distribution of such kind of reconstruction. The precision can
242 be quite high($\sim 50\mu m$) even for DT-distribution with 5k events. This method is limited by
243 core DT-diagram stepping.

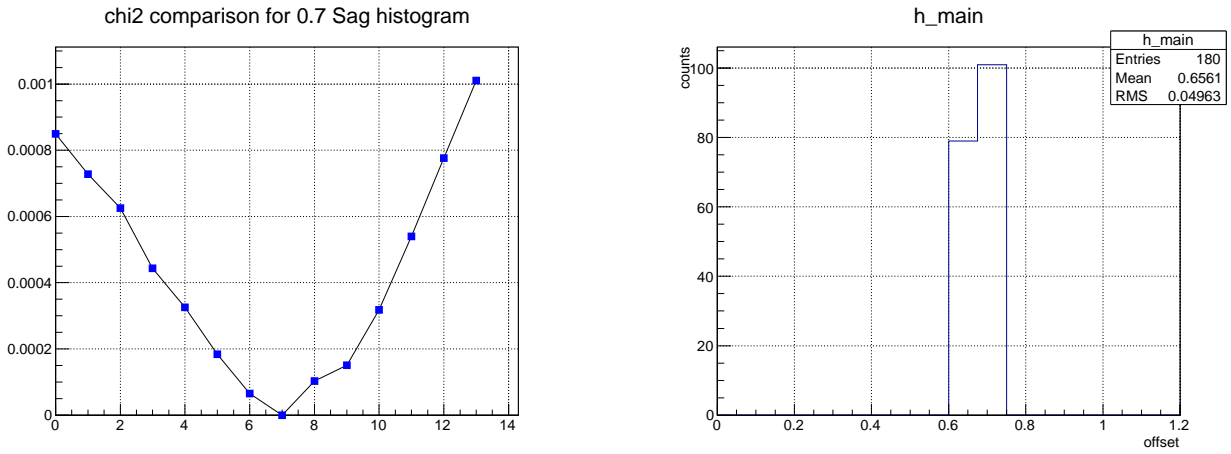
244 **”Minimum of χ^2 as linear approximation”**

245 If dependence of χ^2 criteria of wire displacement S for near to the true position region is
246 linear(that certainly is not a true, but as first approximation) than we can easily find this
247 intermediate value of wire displacement.

248 There we proceed in two steps. The first is raw estimation of wire displacement as in above
249 mentioned method.

250 For the second step we need to know some additional estimations. The first question is how
251 small can be χ^2 in our case? Lets fix statistic on 50k events for one DT-distribution. This
252 value should a bit depend for different S . But for now lets consider that it is a constant value.
253 From the Fig.15a you can see distribution of χ^2 from comparison of 20 DT-distribution⁵ for
254 $S = 0.7mm$. Mean value + RMS of distribution is $5.3 * 10^{-5}$. So if some of the χ^2 is higher
255 than this threshold than we go for second stage.

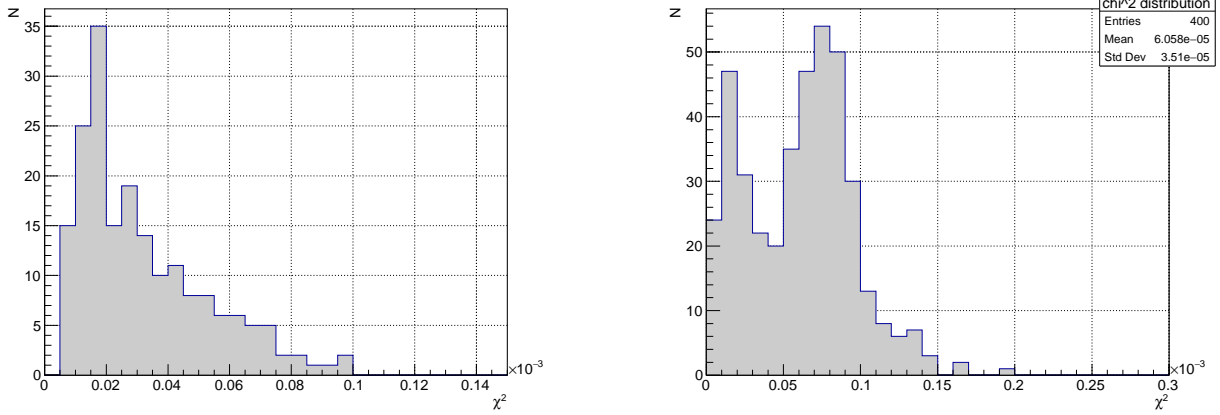
⁵pair comparison give us $C_{20}^2 = \frac{20!}{2!18!} = 190$ different combinations



(a) Series of χ^2 of comparison 0.7mm sag core td-distribution with each of core histograms. 14 core histograms for sag range 0 ... 1.3mm with stepping of $100\mu\text{m}$

(b) Distribution of wire offset reconstruction from 180 series 5k events each. 50k events for *core* template histograms. True bias is 0.63mm. 1 bin = 0.1 mm.

Figure 14: Wire position(displacement) reconstruction



(a) χ^2 distribution of comparison of 20 DT-distributions diagrams each other ($C_{20}^2 = 190$ combinations)

(b) χ^2 distribution of comparison DT-distribution histograms 0.6mm S vs 0.7mm

Figure 15: Comparison of χ^2 distributions for self-comparison of DT-distribution diagram.

In the Fig.14b you can see distribution of wire sag calculation for 180 histograms with 5k events statistic. Precision in this case $\sim 50\mu$. The algorithm of sag estimation is pretty simple: wire offset value is equal to the offset of best matched *core* histogram.

After that we know sag value at series points of the tube. Then we can find whole sag profile as fit of these points by curve with several free parameters.

From the Fig.15b the distribution of χ^2 for adjacent point have narrower distribution by comparison to "self-comparison" χ^2 distribution. Therefore calculation of *S* from analyse of consecutive smallest χ^2 values can improve precision.

264 **6.4 Practical measurements of DT-distribution**

265 We need second detector that can measure position of muon that hit STRAW tube. It can be
 266 Si strip sensor based detector or detector based on scintillation with the same destination.

267 Each kind of detector have it's own advantages and disadvantages. The potential cell unit
 268 (strip or pixel) of Si detector will be smaller than in scintillator but also is much expensive. At
 269 the current stage we deal with 1cm diameter tubes. So scintillator is primal target. But it can
 270 shift to the Si sensors if scintillators will not provide satisfied precision.

271 Preliminary scheme of DT-measurements you can see on the picture Fig.16

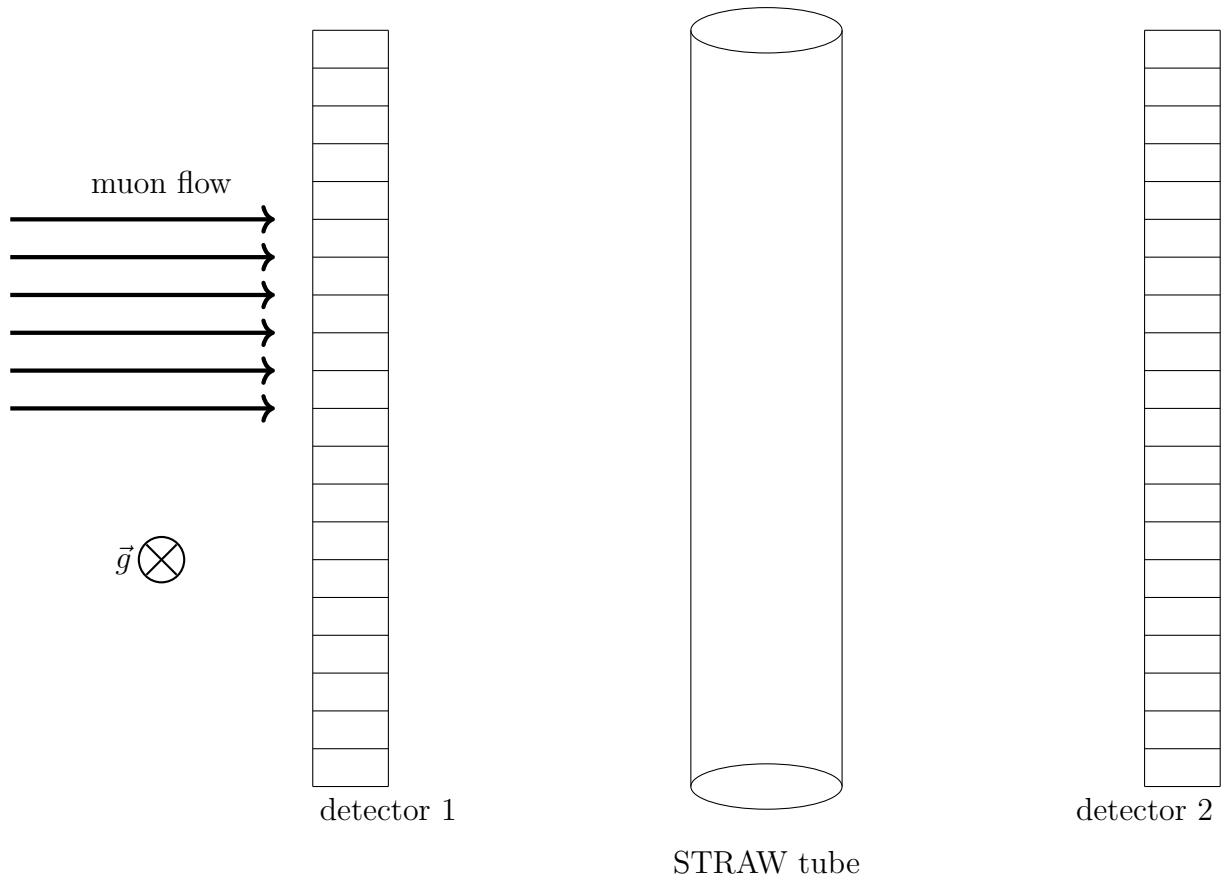


Figure 16: principal layout of measurement of core DT-distribution histogram

272 In this method detector before tube (D1) and detector placed after the tube(D2) in total
 273 should provide sufficient precision for track reconstruction to be able distinguish tracks for
 274 different section of the tube (approximately as shown on the Fig. 13). Muon flow should be
 275 homogeneous and so D1 and D2 also should cover full acceptance of the tube.

276 The profile of the wire sagging can be measured by optical method. Walls of the tube is
 277 very thin, so it can be simplest way to get sag profile.

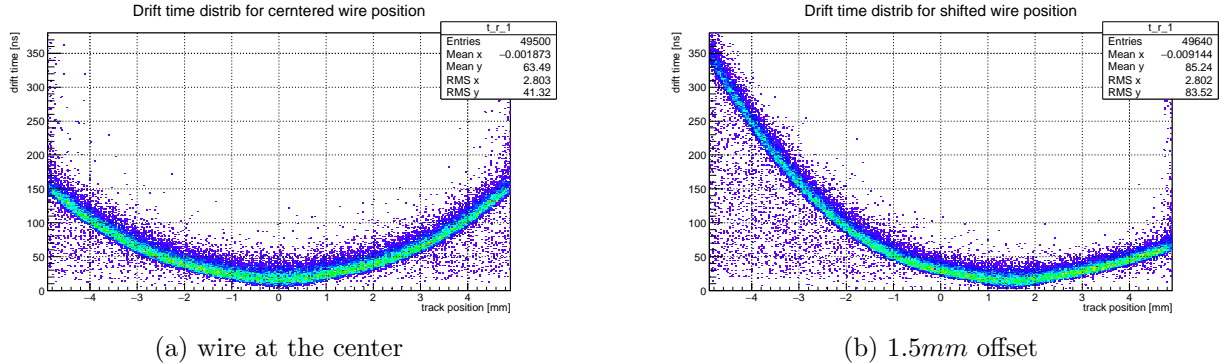
278 7 Track reconstruction

279 The time between the track hit time stamp and the signal rising edge is a measure of *drift time*
 280 of these electrons. The relation between the *drift time* and the distance from the track to the
 281 center of the tube(wire while no sag for centered wire) is called *drift time - distance* relation or
 282 *tr-relation*.

283 The drift time t is a function of track position (relative to the wire) and electric field along
 284 the drift trajectory.

285 One assumes that the working position for straws will be perpendicular to the particle flow,
 286 and acceptance of particle spreading will not be significantly big. So tracks will be collinear
 287 each other within every separate STRAW tube unit.

288 Summing the above mentioned we have one dimension task – reconstruct tracks on vertical
 289 axis⁶ (see examples of outcome tr-distribution $t = t(r, s = 0)$ in Fig.17a and Fig.17b) even the
 290 wire sagging. Sagging will be always down thanks to gravitation force \vec{g} .



(a) wire at the center

(b) 1.5mm offset

Figure 17: Distribution of drift time t_{drift} as function of track position r_{track} relatively to the tube center

291 The rt-relation varies along the tube according to wire displacement s . Thus we have for
 292 the drift time:

$$t_{drift} = t_{drift}(r_{track}, s) \quad (5)$$

293 The idea is to find the inverse dependence

$$r_{track} = r_{track}(t_{drift}, s) \quad (6)$$

294 From Sec.6 we can find sag profile for straw. Therefore the rt-calibration becomes 1 dimen-
 295 sion less for every certain value of wire displacement s_0 :

$$r = r(t, s = s_0) \quad (7)$$

⁶An example of single track reconstruction which explains the approximate procedure of reconstruction you can see on Fig.4

296 7.1 How drift time resolution depends on wire offset?

297 Deformation of electric field inside the tube invoked by wire displacement from the center
 298 position affects drift time. Here we are going to estimate magnitude of drift time change.

299 As was noted above we make a binning for our data along the r_{track} (Fig.17a,17b). Resolution
 300 equals to RMS at every bin of digram (Fig.18).

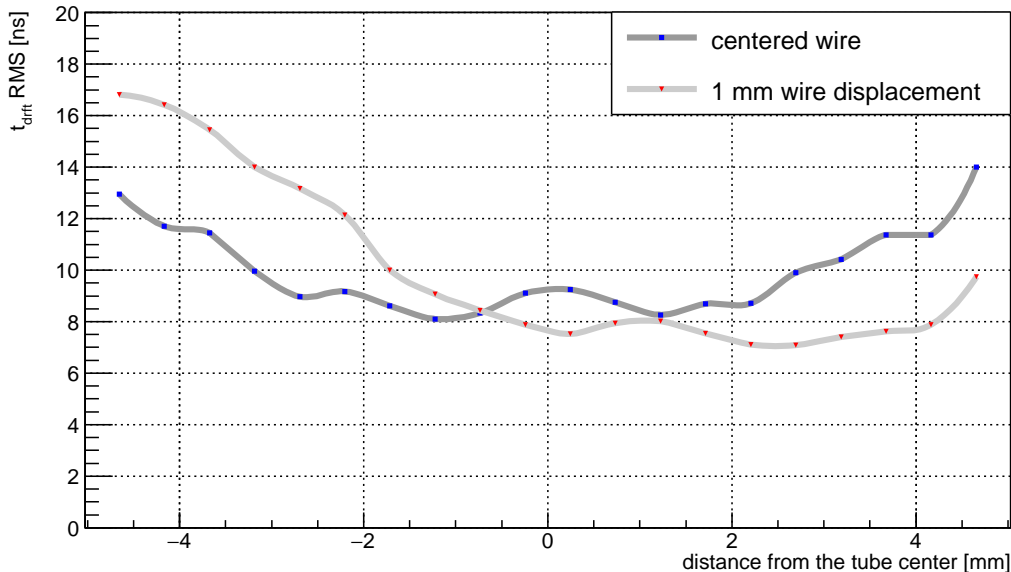


Figure 18: Resolution of drift time as a function of distance from the wire.

301 We are dealing with probabilistic nature of clustering that spread RT-relation from thin
 302 line. The leakage noise is also present in calculation but the effect is not very high (especially
 303 in this calculation).

304 Every plot of output current (see fig. 5) consist of 1000 equidistant frames. The threshold is
 305 set to 5σ of noise. Leakage noise make effect on drift time measurements in case its amplitude
 306 becomes higher than threshold value in range from $t = 0$ to $t = t_{drift}$. At five-sigma there is
 307 only one chance in nearly two million that a random fluctuation would yield the result. The
 308 drift time for tracks close to the tube edge can be up to 150ns and 300ns in case wire displaced.
 309 The probability to meet noise above threshold value is less than 0.02%.

310 Another source of noise points on TR-distribution comes from δ -electrons that cause sec-
 311 ondary ionisation in tube volume. Only those electrons make impact which are emitted in the
 312 direction of the wire(see example on fig.19a).

313 The number of events out of TR-ralation caused by δ -electrons is quite small. Especially
 314 percentage of events where δ -electrons make effect on drift time is less than 1% of total number
 315 of events in GARFIELD simulations.

316 Tube wall is very thin but particle still can cause δ -electrons when crossing it. GEANT4
 317 studies show that such kind effect also presents in interaction of muon with tube volume, and
 318 percentage of events with δ -electron that affect drift time even less than 0.2%.

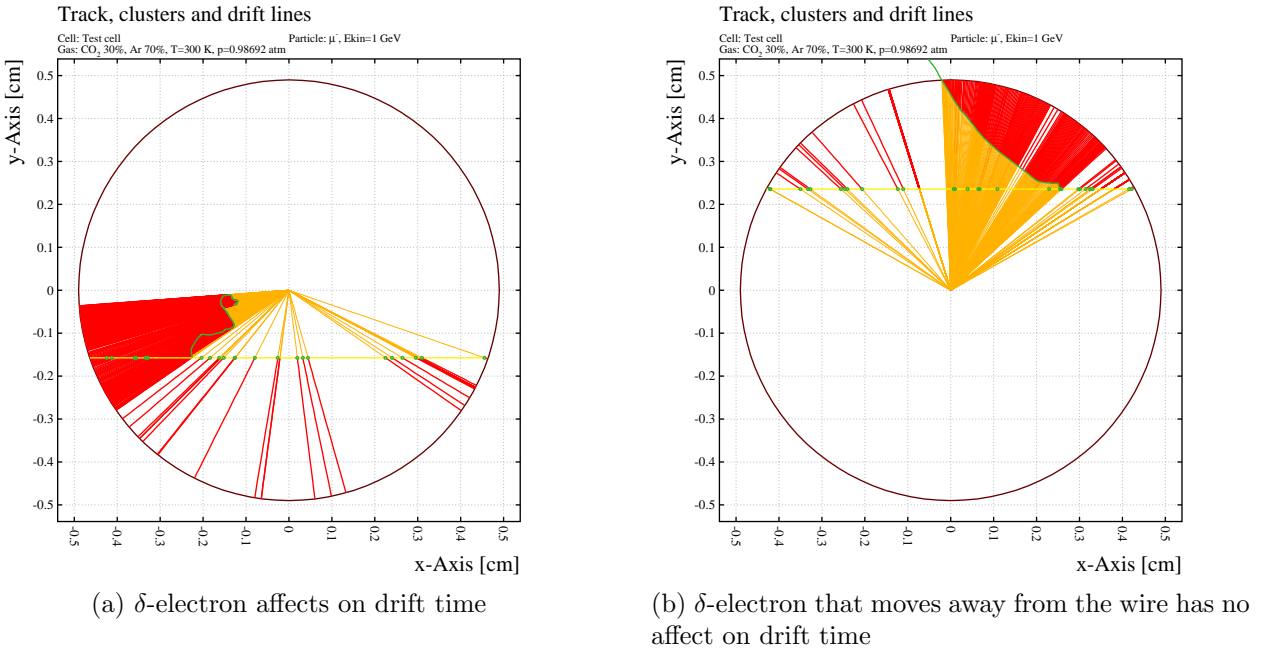


Figure 19: Garfield simulation with δ -electron presence. Red lines - ion trajectory, yellow - electrons. Trajectory of δ -electron marked by green curve line.

319 7.2 Finding of rt-relation

320 The RT-relation depicts relation between drift time and track position. The idea is to find the
 321 best fit of give data to achieve higher resolution and avoid systematic errors.

322 The problem is in that we have to minimize influence of noise while fit. One suppose that
 323 the noise has approximately homogeneous distribution of points that locates below the main
 324 line of distribution. Consequently we can filter it by fitting only points from regions with local
 325 point density higher than some threshold value. Another way is to make a binning of our
 326 distribution along the track position and fit every 1D histogram by Gaussian. The fit points of
 327 Gaussian mean values by fit function.

328 Nevertheless our data contain very small amount of "non-track" points.

329 TR-relation is asymmetry relatively to the $r = 0$ almost in all cases except wire in the center
 330 of the tube. Therefore we have to calibrate for every of branches. It means we need to find two
 331 track positions for every of drift time value and reject one of them in further data processing
 332 stages.

333 In previous section we found way to measure wire sag profile. So we can use this trick in
 334 present stage for separating data into "right" and "left" branch. Every of branches we will
 335 calibrate separately.

336 Lets suppose we can fit every of TR-diagram by pair of analytic fit functions (8):

$$t(r_{track}) = e^{a_0 + a_1 r_{track}} \quad (8)$$

337 If the Fig.20 you can see TR-relation. Fitting is not perfect because of using simple fit
 338 function template (8). But we will use reverse to the (8) relation, because we have to find r_{track}

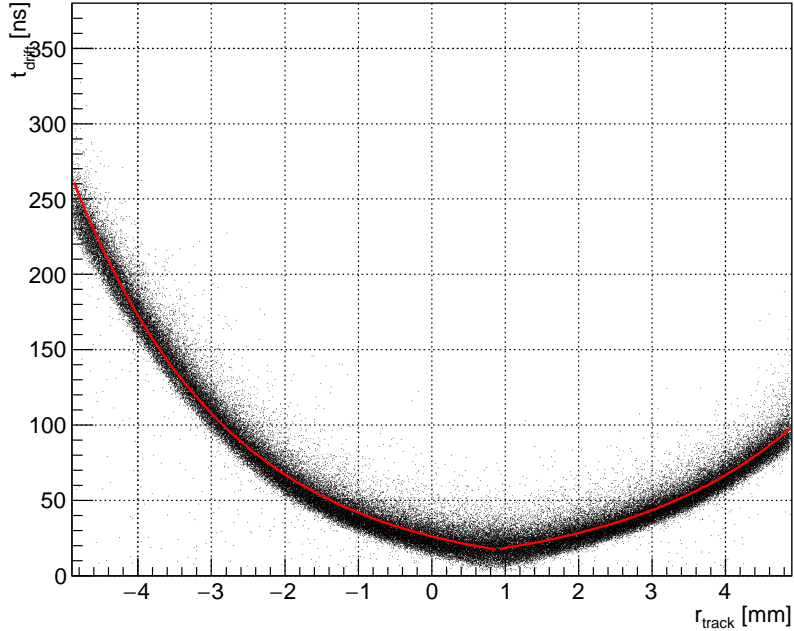


Figure 20: TR-relation fitting for 0.9mm wire offset value

from known t_{drift} . We can do it because the aim of this studies is not a precise calibration but global evaluation effect of wire sagging into total result.

As you can see in the Fig.20 red fit line does not cover whole drift time spectre. So events with drift time less than covered range(less than $\sim 20\text{ns}$) counts as track through the wire:

$$r_{track}(t_{drift} < t_{min}) = r_{wire \ pos} \quad (9)$$

where $t_{min} = \min(t_{drift}(r_{track}))$, $r_{track} = \overline{(-r_{tube}, r_{tube})}$. Respectively tracks with drift time higher than maximum of fit function range is artificially counted as tracks with near tangents to the tube position $r_{track} = \pm r_{tube}$ (because efficiency decreases near the tube wall down to 20%).

7.3 Track reconstruction precision

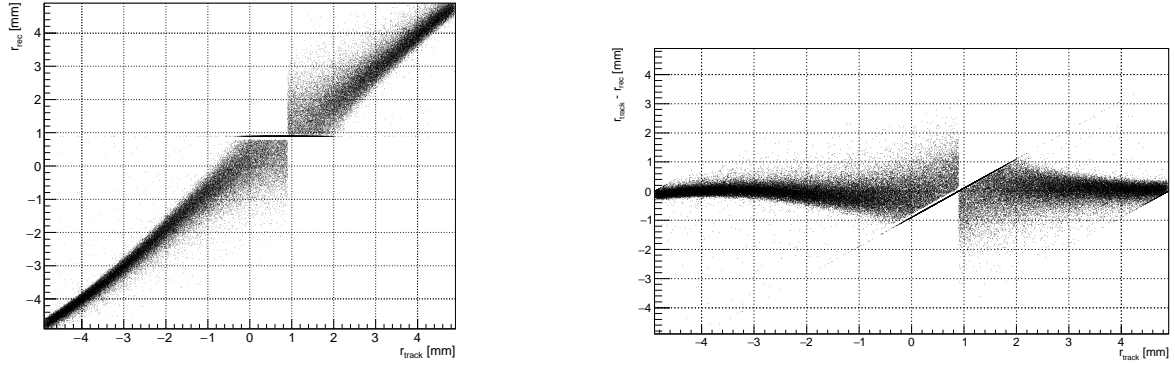
Obviously the precision is the main factor in design of detector.

The STRAW tube tracker should be as light as possible to avoid multiple scattering on structural components of detector. But design should be changed within reason if precision suffers from this⁷.

How precision of track reconstruction depends on wire position(wire displacement)?

As you can see on Fig.22 there are no significant difference of track reconstruction precision between two mode of wire location despite of the increasing drift time for displaced wire position(with almost factor of two). The highest resolution($\sim 0.1\text{mm}$) near the tube wall and

⁷Especially design with no sagging works well for experiment NA62 [1]. But they have more than 2 times shorter straw when tube have insert in the middle of the tube. So sagging becomes negligible in this case.



(a) reconstructed track position r_{rec} as function of true track position r_{track}

(b) $r_{track} - r_{reconstructed}$ as function of r_{track}

Figure 21: Distributions of matching of track position to their reconstructed value.

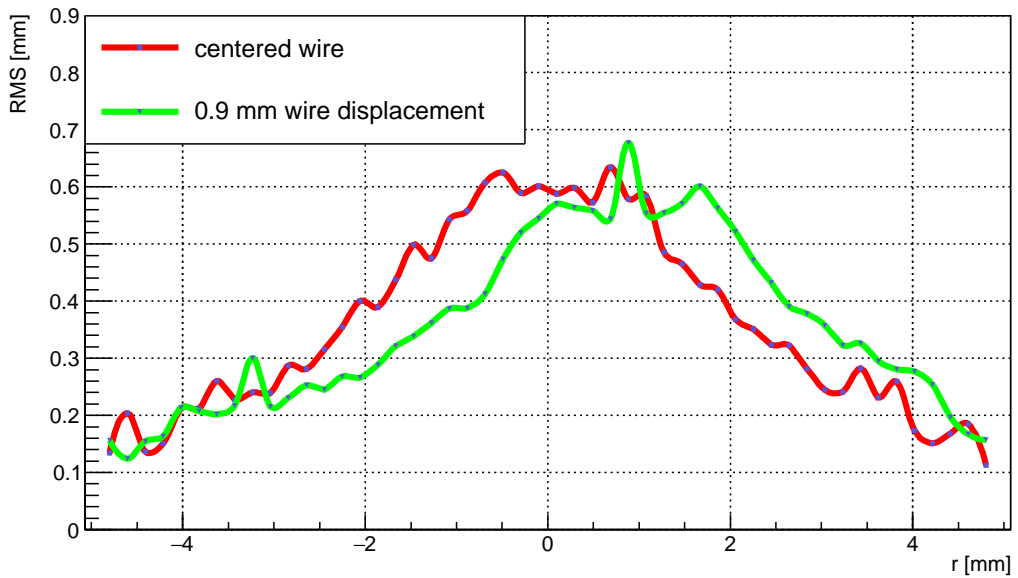


Figure 22: Comparison of track reconstruction precision for two wire position. Value of precision at every point means RMS of data sample near corresponding track position r . Red line corresponds to the centered wire position, green line – to the 0.9mm sagged wire position.

356 worst value $\sim 0.6mm$ is near the wire because the clustering effect. Higher gas pressure should
 357 resolve this problem.

358 8 Measurements

359 We made measurements of some important drift tube parameters. We had tube of $\sim 50\text{cm}$
 360 length. But despite of short tube length we made measurements where the length of the tube
 361 is not important.

362 The tube was manufactured in Dubna(Russian Federation) and was placed into the appropriate
 363 mechanics which include tube fixing, channels for supply of gas mixture, connector for
 364 grounding to the tube walls and connector for High Voltage (HV) supply.

365 The whole system is not compact, therefore we could not avoid the parasitic capacities. Now
 366 we will not go into details about it, as we have nothing to compare with because the system is
 367 non-separable.

368 The scheme of gas supply, circulation and control in the tube is shown in the Fig.23.

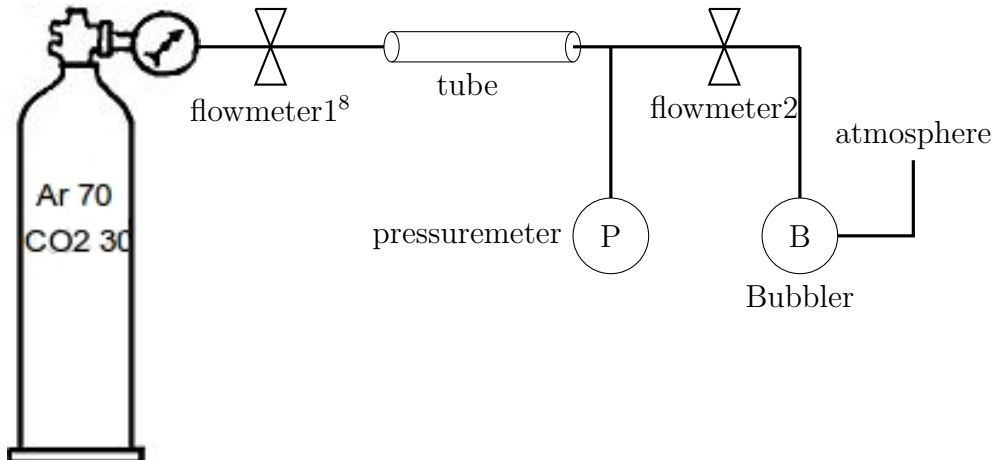


Figure 23: Gas circulation scheme and circuit of connection of flow control through the drift tube

369 The electric scheme of the drift tube connection is shown in the Fig.24.

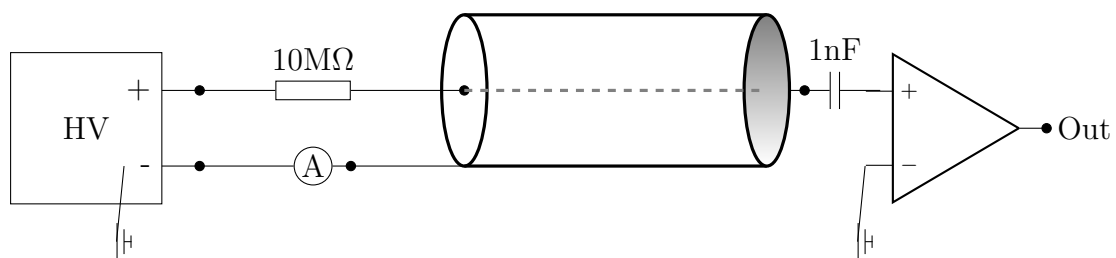


Figure 24: The electric scheme of the drift tube connection

370 As it is seen above, the scheme is very simple.

371 For our research we used a source Fe^{55} which is suitable for a drift tube calibration. In our
 372 case Fe^{55} serves as a photon source with almost monochromatic spectra with energy 5.9 keV.

373 The most important parameter which we have to measure is Gain G (3).

374 The idea is to measure a charge that goes through the tube electric circuit per unit of time
 375 and then find Gain. We assume that a current I_0 through the ampere meter(see fig. 24) is

376 constant when the radioactive source is absent. The current is non-zero when the tube detects
 377 background particles(for example atmospheric muon flux) or when a leakage current is present.
 378 Therefore, with the presence of a source Fe^{55} all surplus of the current $\Delta I = I - I_0$ in the drift
 379 tube circuit occurs because of gamma ray detection.

380 On the other hand, we can write ΔI in terms of initial amount of electrons and Gain in the
 381 following form :

$$\Delta I = GN_0e, \quad (10)$$

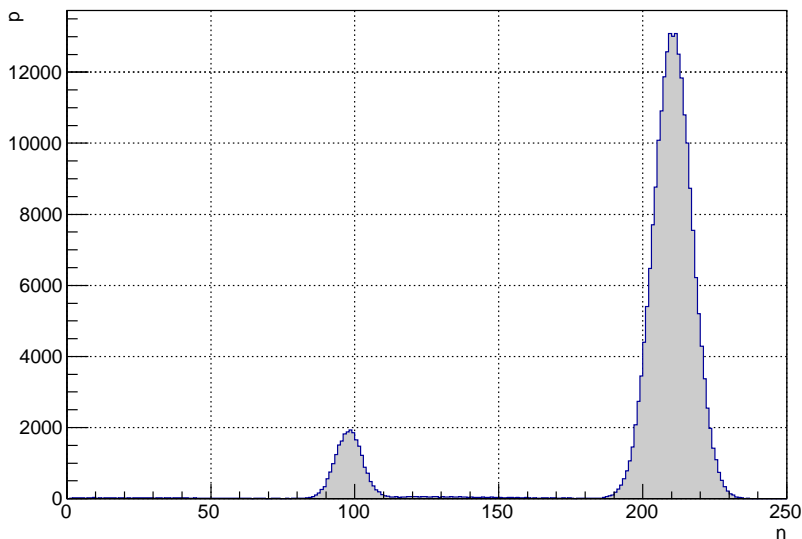
382 where G – Gain; N_0 - number of initial electron-ion pairs per second; e - charge of electron
 383 in C.

384 On the other hand we can express N_0 as:

$$N_0 = R \cdot \langle n \rangle = R \cdot \sum_n np(n) \approx R \int_0^{\infty} np(n)dn; \quad (11)$$

385 where $p(n)$ is a probability that the photon with energy 5.9 keV after interaction with
 386 argon atom will create n electron-ion pairs; R is a rate [Hz], as we need to find the amount of
 387 electron-ion pairs per one second.

388 The calculation of the distribution $p(n)$ in GARFIELD is shown in Fig.???. In the figure
 389 we can see the two peaks: the main photopeak and the smaller escape peak. The escape peak
 390 for argon is known to be 3.2 keV less than the primary peak. An escape peak is formed by
 391 a number of photon interactions in the gas resulting in one primary ionization electron and a
 392 re-emitted X-ray with a long mean free path.



394 Figure 25: $p(n)$ distribution

393 The realisation of a measurement is very simple. On the amplifier output (see Fig.24) the
 394 signal goes to the discriminator with trigger threshold on the level enough for a signal detection
 395 and big enough for noise neglecting. The signal from discriminator in rectangular form goes

396 into counter. The counter is triggered for the rising edge. This scheme has a small dead time
 397 $0.5\mu s$, therefore for the signal frequency of $R \sim 5000 \frac{\text{events}}{\text{second}} \approx 200 \frac{\mu s}{\text{event}}$ the amount of non
 398 counted signals is negligibly small.

399 For the first gain estimation we assume about avalanche superposition and linear amplitude
 400 dependence of final signal on the amount of initial electrons(later we will show that this is not
 401 true).

402 From the distribution in Fig.25 we can find $\langle n \rangle = 197.87$ for average amount of primary
 403 electron because of photon (5.9keV) interaction with atoms of a gas $Ar70\% + CO_230\%$.

404 The results of measurements are shown in the table 3. The Gain curves G(V) for several
 405 pressure values are shown in the Fig.26.

Gain(no cor)	P[bar] (U[V])	HV [V]	Thr [mV]	I [nA]	RMS [nA]	Rate [Hz]
11138	1.0(0.857)	1600		1.7700	0.0919	=
18196	1.0(0.857)	1650		2.8915	0.1598	=
29255	1.0(0.857)	1700	32	4.6490	0.2328	4965.9
47012	1.0(0.858)	1750		7.4707	0.4380	=
73159	1.0(0.857)	1800		11.6257	0.5630	=
9885	1.106(0.906)	1650		1.6921	0.1099	=
15747	1.106(0.905)	1700		2.6955	0.13381	=
25275	1.106(0.905)	1750	32	4.3263	0.1975	5349.0
39887	1.106(0.906)	1800		6.8274	0.2841	=
61359	1.106(0.906)	1850		10.5028	0.4567	=
9260	1.205(0.951)	1700		1.6921	0.1053	
14536	1.205(0.951)	1750		2.6562	0.1274	
22991	1.205(0.951)	1800	32	4.2012	0.1900	5710
35777	1.205(0.951)	1850		6.5376	0.2880	
54684	1.205(0.951)	1900		9.9924	0.5284	
5444	1.309 (0.998)	1700		1.03	0.06	
8351	1.309 (0.998)	1750		1.58	0.14	
13267	1.309 (0.998)	1800		2.51	0.12	
20615	1.309 (0.998)	1850	32	3.90	0.15	5987
31716	1.309 (0.998)	1900		6.00	0.29	
48102	1.309 (0.998)	1950		9.10	0.38	
69987	1.309 (0.998)	2000		13.24	0.50	
100751	1.309 (0.998)	2050		19.06	0.78	

Table 3: Gain measurements

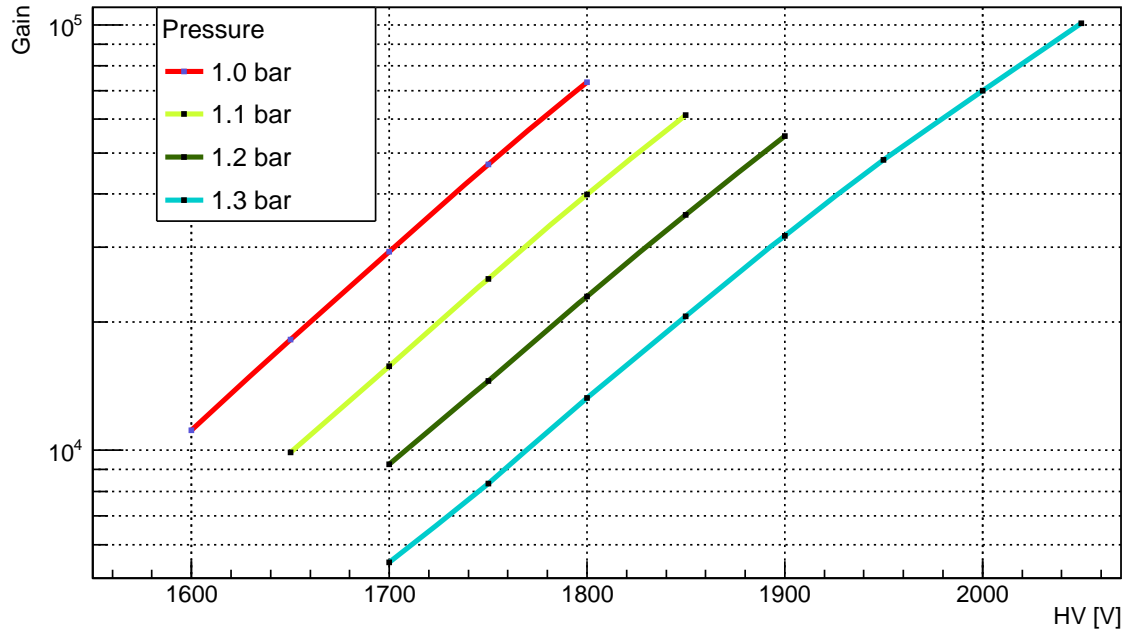


Figure 26: Gain experimental curves for several values of gas pressure in the drift tube.

406 8.1 Experimental spectra from the source Fe55

407 ^{55}Fe is a source of gamma-rays with energy of 5.9 keV. Each signal at the output of amplifier
 408 differs by amplitude in dependence of initial electron number. Therefore, according to the cal-
 409 culated in GARFIELD spectra $p(n)$ (see Fig.25), it is expected to see two peaks in experimental
 410 spectra.

411 For spectra measurements we first have to get a match between a certain signal and the
 412 amplitude on the output of the drift tube. In our case such a quantity is an integral from a
 413 signal on during the time of a signal.

414 The amplified signal from the output of the amplifier is sent in parallel through the linear
 415 splitter to the discriminator and delay system. With the signal from discriminator the sampling
 416 signal and busy signal is formed. During the busy signal the analysing system does not accept
 417 the signal from the drift tube (this is a dead time for this detector system). The delayed
 418 signal from the amplifier integrates during the sampling signal and then digitalizes with 10-bit
 419 ADC. After digitalizing the signal is sent through the optical channel to PC, where the data is
 420 recorded into separate ROOT-file.

421 The stages *sampling + storing* are time-consuming and a dead time in this case is bigger than
 422 an average time interval between events in the tube (with current detector system) therefore is
 423 a big probability to miss detecting an event.

424 The sampling stage is built in such a way to calibrate for pedestal shelf voltage from the
 425 integrator. On the final histogram it will look as a small peak. We will calibrate exactly with
 426 regard to it. The second control point is a gamma-ray 5.9 keV photo peak from the source
 427 ^{55}Fe .

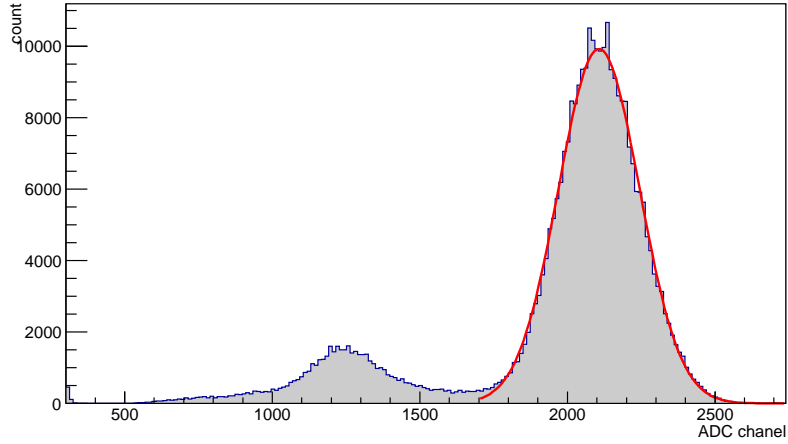


Figure 27: Experimental spectra from ^{55}Fe .

point of reference	channel	electrons per cluster(simulations)
zero pedestal (<i>gauss</i> $\mu \pm \Delta\mu$)	301.1 ± 0.3	0
5.9 keV	2107.4 ± 0.3	210.42 ± 0.01
escape peak	1253.3 ± 0.9	97.99 ± 0.03

Table 4: Coordinates of peaks from Fig.27 and Fig.25

428 8.2 Space charge effect

429 Photons from ^{55}Fe of energy 5.9 keV create ~ 200 electron-ion pairs as a result of photoeffect
 430 with $Ar70\% + CO_230\%$ gas mixture. As we have a strong electric field between anode and
 431 cathode such electron cloud starts to drift toward a wire. The external field distorts as any
 432 space charge creates its own e/m field. As a result, partial avalanches per initial electron of
 433 a cloud creates an avalanche of size smaller than from a single-electron cloud(as in case muon
 434 ionisation).

435 Such an effect indeed was observed. If we suppose a linear dependence of output signal
 436 amplitude from number of initial electrons a relative position for experimental peak should be
 437 located at(calibration relatively to the photopeak):

$$channel_{escapePeak} = \frac{2107.4 - 301.1}{210.42} 98 + 301.1 = 1142.3 \neq 1253.3, \quad (12)$$

⁴³⁸ **9 Appendix**

⁴³⁹ **9.1 pressure meter**

⁴⁴⁰ For the pressure measurement inside of drift tube we used pressure transmitters from
⁴⁴¹ SensorTechnics[®]. The devise is marked by ID:CTE9005AQ4, so we used appropriate datasheet
⁴⁴² from the manufacturer [5].

⁴⁴³ According to datasheet and marking, this pressure transmitter is designed for pressure mea-
⁴⁴⁴ surements in the interval $0 \dots 5 \text{ bar}$. But on the transmitter is marked an interval $0 \dots 3,5 \text{ bar}$.
⁴⁴⁵ So to be able to use this device, we additionally calibrated it.

⁴⁴⁶ For this purpose we used two control points: the output current value for atmospheric
⁴⁴⁷ pressure at that point (727 mmHg) and a current for a vacuum. To get a vacuum we used a
⁴⁴⁸ pump which decreases a pressure to the value $< 0.001 \text{ bar}$ which we consider as a vacuum.

Table 5: Control points for calibration of pressure transmitter.

pressure [bar]	voltage[V]
< 0.001	0.405
1	0.858

⁴⁴⁹ Therefore the voltage dependence taken on a resistor 100Ω depends on a pressure as:

$$V = 4.05 + 0.453 \cdot P[\text{bar}] \quad (13)$$

$$P[\text{bar}] = -0.894 + 2.2075 \cdot V \quad (14)$$

450 **References**

- 451 [1] F. Hahn, F. Ambrosino, A. Ceccucci, H. Danielsson, N. Doble, F. Fantechi, A. Kluge, C.
452 Lazzeroni, M. Lenti, G. Ruggiero, M. Sozzi, P. Valente, and R. Wanke. NA62: Technical
453 Design Document. Technical Report NA62-10-07, CERN, Geneva
- 454 [2] SHiP Technical Proposal from 8 april 2015: arXiv:1504.04956v1
- 455 [3] GARFIELD tutorial <http://garfield.web.cern.ch/garfield>
- 456 [4] Outer Tracker calibration and open charm production cross section measurement at LHCb,
457 2013 A.V.Kozlinskiy.
458 <http://dspace.ubvu.vu.nl/bitstream/handle/1871/40430/dissertation.pdf>
- 459 [5] DataSheet for Pressure transmitters for corrosive liquids and gases CTE/CTU9000 series.
460 http://www.first-sensor.com/cms/upload/datasheets/DS_Standard-CTE-CTU9000_E_11509.pdf
- 461 [6] W. Bonivento, A. Boyarsky, H. Dijkstra, U. Egede, M. Ferro-Luzzi, B. Goddard, A. Golutvin,
462 D. Gorbunov, R. Jacobsson, J. Panman, M. Patel, O. Ruchayskiy, T. Ruf, N.
463 Serra, M. Shaposhnikov, and D. Treille. Proposal to Search for Heavy Neutral Leptons at
464 the SPS. Technical Report CERN-SPSC-2013-024. SPSC-EOI-010, CERN, Geneva (Oct,
465 2013).
- 466